Elucidating the Effect of Al_2O_3/SiO_2 Mass Ratio upon SiO_2-MnO-CaF_2-Al_2O_3-Based Welding Fluxes: Structural Analysis and Thermodynamic Evaluation

Zhanjun Wang [a,b], Zuohong Li [a,b], Ming Zhong [a,b], Zushu Li [c], Cong Wang [a,b] *

[a] Key Laboratory for Ecological Metallurgy of Multimetallic Mineral (Ministry of Education), Northeastern University, Shenyang 110819, Liaoning, China

[b] School of Metallurgy, Northeastern University, Shenyang 110819, Liaoning, China

[c] WMG, University of Warwick, Coventry, CV4 7AL, United Kingdom

*Corresponding author: wangc@smm.neu.edu.cn (C. Wang)

Tel.: +86 15702435155; Fax: +86 24 23906316

Abstract

The effect of Al_2O_3/SiO_2 mass ratio has been fully investigated upon SiO_2-MnO-CaF_2-Al_2O_3-based fluxes by examining weld metal and slag shell morphologies. It has been documented that flux viscosity could be significantly diminished by elevating the Al_2O_3/SiO_2 mass ratio from 0.1 to 0.6, after which only negligible changes are observed. The compositional dependence of flux behaviors has been elaborated by means of structural analysis via Fourier Transform Infrared spectroscopy, Raman spectroscopy and molecular dynamics simulation. The formation of [AlO_4]-tetrahedral units and Al-O-Si with weaker bond energy are encouraged, which is accompanied by the increased NBO/Si (non-bridging oxygen per [SiO_4] units) and decreased Q^3/Q^2 (X_3/X_2) to establish a depolymerized aluminosilicate network. Thermodynamic evaluations have also been performed, showcasing activity and excessive free energy variations to enrich

the structural analysis. Gaining an insight into the physicochemical properties of fluxes from structural and thermodynamic analysis view is essential to empower fundamental understandings towards quality manufacturing.

Keywords: Welding flux; Slag; Viscosity; Structure; Thermodynamic evaluation

1. Introduction

High heat input submerged arc welding (SAW) technique has been widely applied to further improve welding efficiency in the processes of joining high-pressure vessels, oil and gas pipelines, and shipbuilding steels, etc. [1, 2]. Appropriate welding fluxes should be designed to perform intrinsic functions, including covering the welding pool, preventing atmosphere and moisture contamination, and affecting the mechanical properties of high-strength steel by disposing alloying elements transfer from the flux to the weld metal (WM) [3]. High-temperature viscosity is one of the fundamental physicochemical properties that should be carefully considered in the design of high heat input SAW fluxes [4]. Under the stirring action of the plasma arc, extremely intricate slag-metal reactions would occur in the high-temperature molten pool, where the viscosity governs the spreadability of molten fluxes on the WM and dictates mass transfer behavior during crystallization to alter alloying element transfer. Furthermore, viscosity will also affect the appearance of the weld joint [5, 6]. On the one hand, excessive viscosity of the flux prevents the slag from spreading evenly on the surface of the molten pool, forming a weld joint with a narrow melting width, and gases generated during the reaction are not capable of escaping instantly, resulting in

unexpected population of defects, such as pores and slag entrapment [7, 8]. On the other hand, overly low viscosity may exacerbate slag fluidity, posing a challenge to properly protect the weld pool [9].

Si and Mn are fundamental alloying elements in low-carbon low-alloy steels, and reasonably-controlled alloy composition could improve the mechanical properties of the WM [5]. SiO_2-MnO-based welding fluxes are commonly employed to decompose and facilitate the release of O, Si and Mn elements under the action of arc plasma, which can be ultimately transferred to the WM through slag-metal reaction [10, 11]. However, only limited investigations have been reported on the viscosity of SiO_2-MnO-based welding fluxes [12-14]. Available studies suggested that the viscosity of the welding fluxes should be controlled to ensure excellent weld formability. When designing flux, CaF_2 is commonly added to minimize O potential [15-17]. It is accessible that Al_2O_3, by acting as a beneficial ingredient that could significantly improve slag detachability [14], is used to substitute SiO_2 to avoid excessive O to be transferred to the WM. However, excessive substitution of SiO_2 with Al_2O_3 may promote the slag system to be altered from a silicate-based structure to an aluminosilicate-based structure or even an aluminate-based structure, thereby affecting its physicochemical properties. However, the substitutional effects of SiO_2 with Al_2O_3 on the structure of fluxes with wide ranges of Al_2O_3/SiO_2 mass ratios in SiO_2-MnO-CaF_2-Al_2O_3 fluxes have yet to be fully understood. Moreover, revealing the structure of SiO_2-MnO-CaF_2-Al_2O_3 flux system may further elaborate the amphoteric role of Al^{3+} in the fluxes and elucidate the synergistic effect of SiO_2 and Al_2O_3 on the viscosity change, which is essentially driven

by thermodynamics [18].

In this study, the substitutional effect of SiO_2 with Al_2O_3 on the WM and slag shell morphologies upon SiO_2-MnO-CaF_2-Al_2O_3 flux has been investigated and correlated with viscous behavior and flux structure. Various spectroscopic methods, such as Fourier Transform Infrared spectroscopy (FTIR) and Raman spectroscopy, have been employed to determine the structure of fluxes and to identify their distinctive ionic structural units. The results were further corroborated *via* molecular dynamics (MD) simulation and thermodynamic evaluation. It aims to provide fundamentals to ultimately contribute to the understanding of the design of the desired optimal SiO_2-MnO-based high heat input SAW fluxes.

2. Experimental

2.1 Sample preparation

Table 1 Chemical compositions (wt.%) of the designed fluxes.

Sample	Pre-experimental				Post-experimental				Al_2O_3/SiO_2
	SiO_2	MnO	CaF_2	Al_2O_3	SiO_2	MnO	CaF_2	Al_2O_3	
F1	50.00	25.00	20.00	5.00	49.53 (±0.54)	25.45 (±0.24)	19.59 (±0.61)	5.43 (±0.31)	0.10
F2	42.00	25.00	20.00	13.00	42.21 (±0.49)	25.83 (±0.62)	19.26 (±0.33)	12.70 (±0.41)	0.30
F3	34.00	25.00	20.00	21.00	34.82 (±0.41)	24.86 (±0.37)	20.23 (±0.28)	20.09 (±0.32)	0.60
F4	29.00	25.00	20.00	26.00	28.96 (±0.33)	25.34 (±0.43)	19.69 (±0.57)	26.01 (±0.34)	0.90
F5	25.00	25.00	20.00	30.00	24.68 (±0.36)	25.31 (±0.31)	20.14 (±0.23)	29.87 (±0.53)	1.20
F6	22.00	25.00	20.00	33.00	22.21 (±0.28)	25.48 (±0.76)	19.77 (±0.42)	32.54 (±0.21)	1.50

Quaternary SiO_2-MnO-CaF_2-Al_2O_3 fluxes were designed and prepared with reagent grade chemicals of SiO_2 (> 99.7 wt.%), MnO (> 99.8 wt.%), CaF_2 (> 98.5 wt.%), and Al_2O_3 (> 99.8 wt.%) (all from Sinopharm Chemical Reagent Co., Ltd) through standard melting and quenching processes. The chemical powders were dried in a resistance furnace for 2 hours at 800 °C before mixing to remove potential crystalline hydrate. 1000 g powders were thoroughly mixed according to the target mass ratio shown in Table 1. To ensure homogeneity, these fluxes were pre-melted at 1550 °C in a graphite crucible with a matching lid for 30 mins under 0.5 L/min of Ar (99.999 vol%) gas. Afterwards, the pre-melted fluxes were quenched by water, and the collected fluxes were dried at 400 °C for 2 hours to remove moisture and ground for subsequent analysis. The compositions of the quenched samples were measured by X-ray fluorescence (XRF, ZXS Priums II, Rigaku, Japan) and ethylene diamine tetraacetic acid (EDTA) titration method, and the results are provided in Table 1, where negligible change was exposed between the pre- and post-melting. The crystalline state of the quenched fluxes was characterized by X-ray diffraction (XRD, D8 Advance, Bruker, Germany). Figure S1 in Supplemental Materials has confirmed the amorphous state of the fluxes, which indicates that all samples have been well quenched with respective compositional uniformity and structural details preserved at high temperatures [19].

2.2 Submerged arc welding

Bead-on-plate double-wires single-pass SAW (Aotai Electric Power MZS-1000/1250, Aotai Electric, China) was employed with a horizontal travel speed of 500

mm/min and a total heat input of 60.0 kJ/cm (DC-850A/32V for electrode forward, AC-625A/36V for electrode backward). EH36 shipbuilding steel plate was used as the base metal in the welding process. The fluxes and the base metal were prepared according to standard procedures. Other details of the welding process can be referred to the literature [7].

2.3 Viscosity measurements

Viscosity measurement was conducted using a digital rheometer (LVDV-II+; Brookfield Engineering Laboratories, Middleboro, MA, USA). The temperature of the apparatus was controlled by a B-typed thermocouple embedded in the constant hot zone of the furnace. 120 g of fully mixed fluxes were filled into a molybdenum crucible (Inner diameter = 40 mm, Height = 100 mm) and placed within the constant temperature zone of the resistance furnace. The fluxes were heated at 1550 °C for 30 mins to be homogenized before viscosity measurement. The viscosity was measured at 25 °C intervals, and each target temperature was maintained for 20 minutes to achieve thermal equilibrium in the flux. During the entire viscosity measurement, circulating water and Ar gas (99.999 vol%) were introduced to cool the furnace and prevent the oxidation of the crucible and the viscosity apparatus. Pertinent details of viscosity measurements can be referred elsewhere [14, 20, 21].

2.4 Structural analysis from an experimental study

FTIR and Raman spectroscopy have been commonly employed to obtain semi-quantitative structural information of amorphous fluxes. FTIR analysis (Vertex 70,

Bruker, Germany) was carried out at room temperature, and corresponding spectra were collected in the range of 400-1600 cm^{-1}. Raman analysis was carried out with a multichannel modular triple Raman system (LabRAM HR800, Horiba, USA) equipped with a confocal microscope, where a laser with a wavelength of 532 nm was chosen as the excitation source. Measured Raman spectra frequency was from 400 to 1600 cm^{-1} with a precision of 1 cm^{-1}.

2.5 Structural analysis from molecular dynamics simulation

MD simulation was performed using the LAMMPS package to complement the experimental structural analysis [22, 23]. The Born-Mayer-Huggins (BMH) potential was applied to simulate the interaction between adjacent atoms, which can be expressed as follows [22, 23],

$$U_{ij}(r_{ij}) = \frac{q_i q_j}{r_{ij}} + A_{ij}\, exp(-B_{ij} \cdot r_{ij}) - \frac{C_{ij}}{r^6} \quad (1)$$

where $U_{ij}(r_{ij})$ is the interatomic-pair potential for atoms *i* and *j* with a distance of r_{ij}, q_i and q_j are the charges of *i* and *j*, and A_{ij}, B_{ij}, and C_{ij} are the energy parameters specific to the type of atoms *i* and *j* (Supplemental Materials Table S1). During simulation, approximately 5,000 atoms were randomly placed in a three-dimensional periodic boundary model box (Supplemental Materials Table S2 and Figure S2). Atomic dynamic equilibrium at 1550 °C was simulated using the canonical ensemble (Number-Volume-Temperature system) to obtain trajectories for microstructural analysis. Additional simulation details can be found elsewhere [24].

3. Results and Discussion

3.1 Macrographs of weld metals and matching slag shells

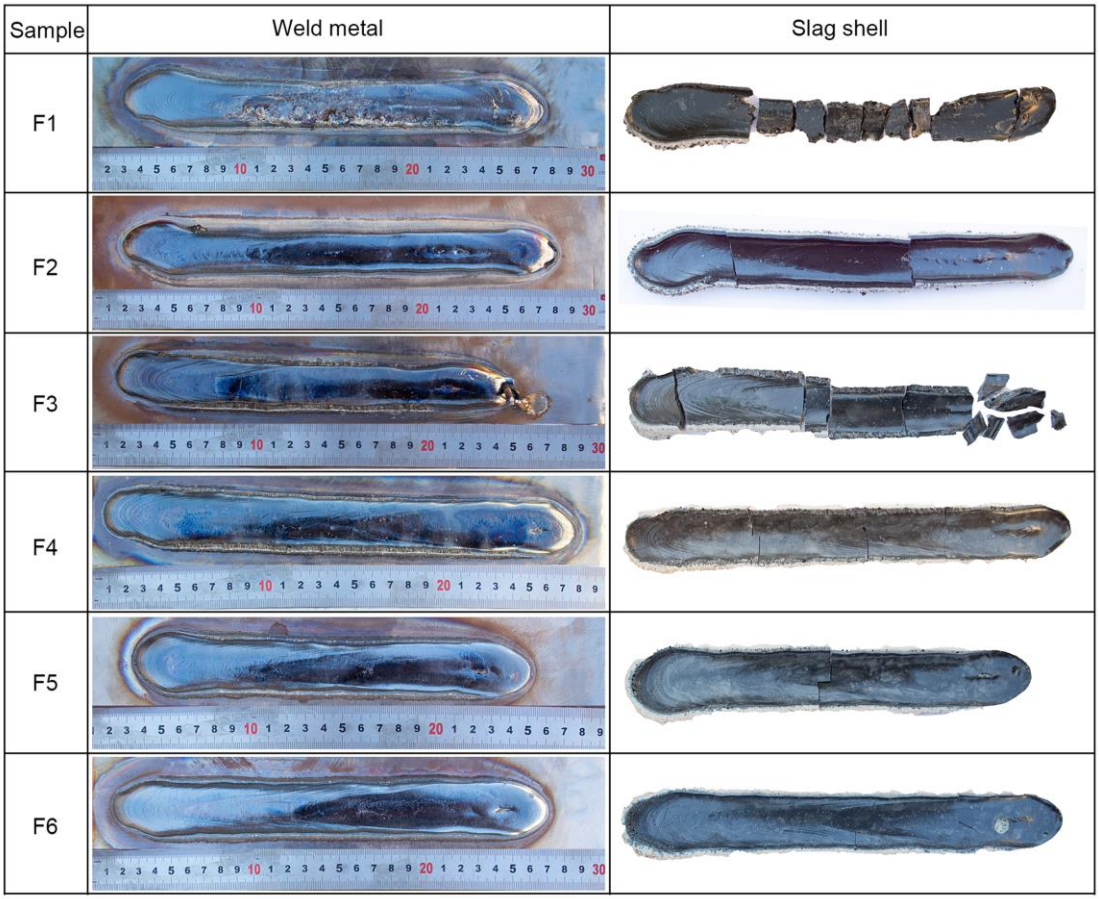

Figure 1 Macrographs of WMs and corresponding separated slag shells treated by different fluxes.

Figure 1 shows that the base metals treated with various fluxes (as listed in Table 1) exhibit different welding features. It appears that the surface quality of WMs improves as the Al_2O_3/SiO_2 mass ratio increases, which is concurrent to slag shell internal surfaces morphing from fine to coarse ripples. The most striking phenomenon is that the WM corresponding to sample F1 shows extremely poor slag detachability.

This may be due to the formation of molten slag with high viscosity, which leads to the failure of the welding flux to spread in time or the failure of the impurities involved to rise during welding [25, 26].

3.2 Viscosities

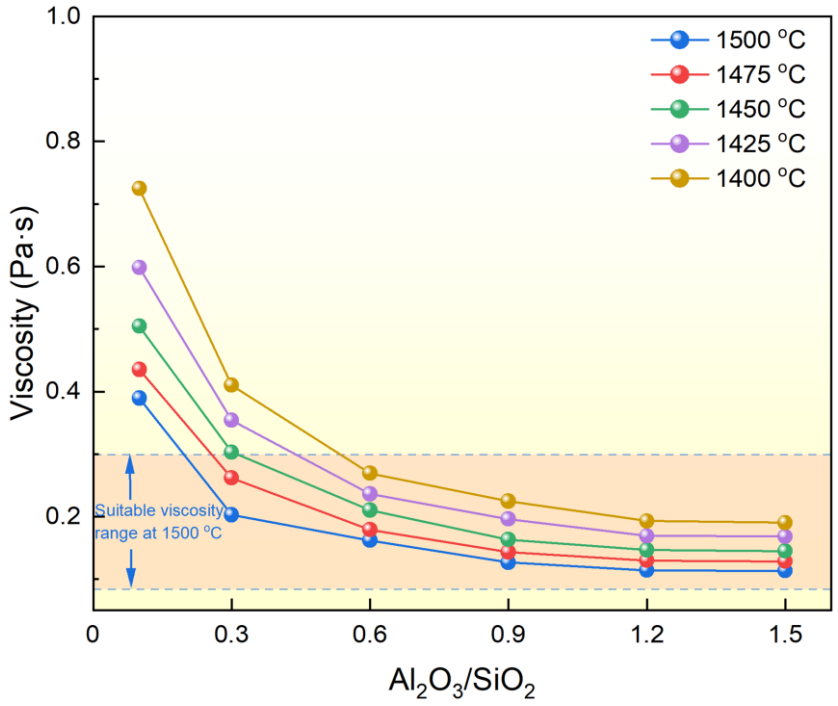

Figure 2 Viscosity of SiO_2-MnO-CaF_2-Al_2O_3 fluxes as a function of Al_2O_3/SiO_2 mass ratio obtained at various temperatures.

Figure 2 shows measured viscosity values of SiO_2-MnO-CaF_2-Al_2O_3 fluxes as a function of the Al_2O_3/SiO_2 mass ratio. Generally speaking, as the Al_2O_3/SiO_2 mass ratio increases from 0.1 to 1.5, the overall viscosity presents a decreasing trend, which is consistent with the trajectory reported previously [27]. It is noted that the viscosity drops sharply at the Al_2O_3/SiO_2 mass ratios from 0.1 to 0.6, while the downtrend retards extremely with further increasing the Al_2O_3/SiO_2 mass ratio to 1.5. Furthermore, the

viscosity change seems to be negligible above 1450 °C for fluxes with Al_2O_3/SiO_2 mass ratios higher than 0.9. According to Jackson et al. [28] and Singh et al. [29], at 1500 °C, flux viscosity should be controlled within 0.08-0.3 Pa·s, as displayed in the shaded area in Figure 2, to ensure adequate weld formability [14]. Based on the above discussion, the appropriate Al_2O_3/SiO_2 mass ratio for this series of fluxes should be controlled above 0.3 [30, 31]. To further illustrate the above viscosity variation trend, the structure of the flux is subsequently explained in detail.

3.3 FTIR and Raman structural analysis

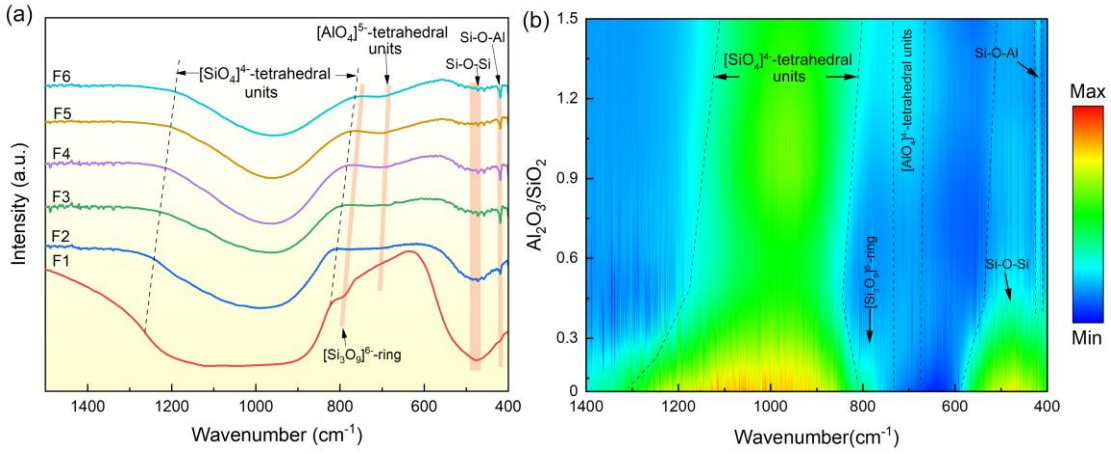

Figure 3 (a) FTIR absorption spectra of all SiO_2-MnO-CaF_2-Al_2O_3 fluxes with various Al_2O_3/SiO_2 mass ratios, and (b) FTIR intensity contour map of SiO_2-MnO-CaF_2-Al_2O_3 fluxes.

Figures 3 (a) and (b) illustrate the FTIR absorption spectra and the corresponding intensity contour map of SiO_2-MnO-CaF_2-Al_2O_3 fluxes, respectively. As can be seen, dominant Si-O symmetric stretching vibration bands in the [SiO_4]-tetrahedral units exist between the wavenumbers of 800-1200 cm^{-1} [32]. Due to the lower absolute

concentration of SiO_2, the whole [SiO_4]-tetrahedral symmetric stretching vibration band becomes less pronounced, and the entire vibration band moves to a lower wavenumber position, indicating depolymerization of the aluminosilicate structure with increasing Al_2O_3/SiO_2 mass ratio [33, 34]. Meanwhile, the [AlO_4]-tetrahedral symmetric stretching band gradually appears within a wavenumber range of 600-800 cm^{-1}, which was progressively enhanced with increasing Al_2O_3/SiO_2 mass ratio. Besides, the relative intensity of the Si-O-Si bending vibration peak at 480 cm^{-1} is surprisingly strong for F1 [4]. From F1 to F6, the Si-O-Si bending vibration seems to become slightly weaker until it almost disappears, which is accompanied by the enhanced bending vibration of Si-O-Al located in the wavenumber of ~420 cm^{-1} [27, 35]. In addition, a weak infrared band of $[Si_3O_9]^{6-}$-ring structural units located at ~780 cm^{-1} appears when the Al_2O_3/SiO_2 mass ratio is lower than 0.3 (F1 and F2), but disappears when the Al_2O_3/SiO_2 mass ratio exceeds 0.3 (F3 and F6), suggesting the transformation of complex [SiO_4]-related units to simpler ones [32].

It can be seen that, although the flux changes from a silicate structure to a more complex aluminosilicate structure, decreased relative content of [SiO_4]-tetrahedral units and lower intermolecular force in [AlO_4]-tetrahedral unit would altogether lead to the weakening of the overall structural unit strength.

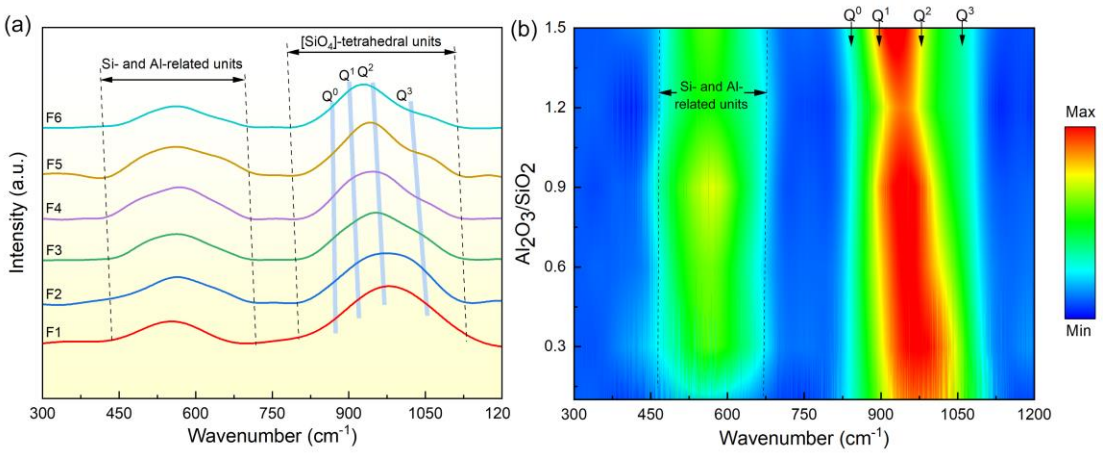

Figure 4 (a) Raman spectra of the fluxes with various Al_2O_3/SiO_2 mass ratios, and (b) Raman intensity contour map of SiO_2-MnO-CaF_2-Al_2O_3 fluxes.

Raman spectra of SiO_2-MnO-CaF_2-Al_2O_3 fluxes after background subtraction are shown in Figure 4 (a). The high-frequency region of the spectral curves at 800-1200 cm^{-1} corresponds to the $[SiO_4]$-tetrahedral units with varying amounts of oxygen anions [3, 22]. Characteristic peaks of the Raman shift near ~860 cm^{-1}, ~900 cm^{-1}, ~960 cm^{-1}, ~1050 cm^{-1} correspond to Q^0 (NBO/Si=4, $[SiO_4]^{4-}$, monomer), Q^1 (NBO/Si=3, $[Si_2O_7]^{6-}$, dimmer), Q^2 (NBO/Si=2, $[Si_2O_6]^{4-}$, chain), Q^3 (NBO/Si=1, $[Si_4O_{11}]^{6-}$, sheet), respectively (Q^i, *i* is the bridging oxygen per $[SiO_4]$-tetrahedral unit; NBO/Si is the non-bridging oxygen per $[SiO_4]$-tetrahedral unit) [36]. "The emerged peaks at the low-frequency region of 400-700 cm^{-1} can be assigned to the overlapped bending vibrations of Si- and Al-related structural units, whereas specific structural information is still under debate [37, 38]. Thus, only the high frequency region associated with $[SiO_4]$-tetrahedral units, which can semi-quantitatively reflect the change of polymerization degree, was employed for subsequent analysis. The overall shift of Raman peaks

towards to the low-frequency region exhibited in Figure 4 (b) demonstrates the depolymerization trend of the entire flux structure, which highly depends on the conversion of cross linkages within the [SiO_4]-tetrahedral units. This is consistent with the result observed by McMillan et al. [39] that the connection of alumina and silicate to form aluminosilicate structure could facilitate the shift of the [SiO_4]-tetrahedral unit peaks to lower frequency regions.

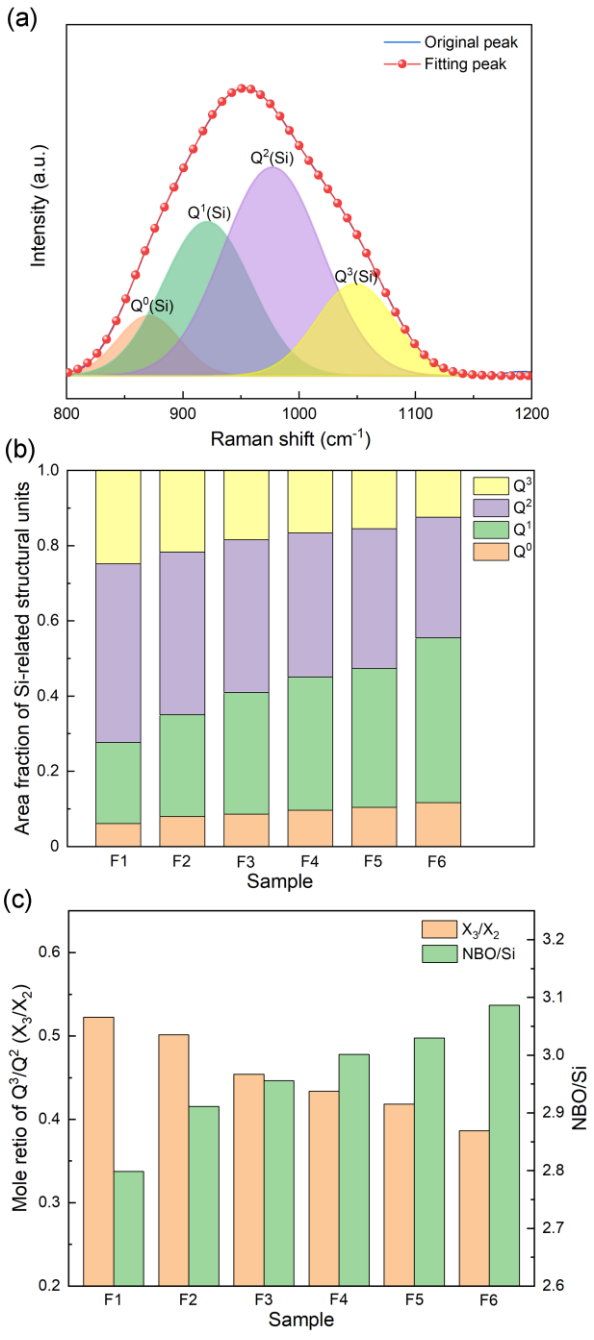

Figure 5 (a) Typical deconvolution result of Raman spectra, (b) area fraction of the characteristic [SiO_4]-tetrahedral units, and (c) variation of NBO/Si and Q^3/Q^2 mole ratios in SiO_2-MnO-CaF_2-Al_2O_3 fluxes.

The integrated areas of different characteristic peaks could provide a semi-quantitative method to decipher respective amount of characteristic structural units in the fluxes. A typical deconvolution result of the Raman spectra was performed by Gaussian function with the minimum correlation coefficient $R^2 \geq 0.999$, as shown in Figure 5 (a) (The deconvolution results of the Raman spectra for all fluxes can be found in Supplemental Materials Figure S3). Figure 5 (b) illustrates area fractions of characteristic [SiO_4]-tetrahedral units. It suggests that area fractions of Q^0 and Q^1 increase as the Al_2O_3/SiO_2 mass ratio is enhanced. In contrast, area fractions of Q^2 and Q^3 decrease accordingly, indicating the transformation of the intricate structural units to more simplified structural units.

Furthermore, the degree of polymerization of the flux structure is inversely proportional to NBO/Si and is proportional to the mole ratios of Q^3/Q^2 [40, 41]. The value of NBO/Si can be calculated by Equation (2):

$$NBO/Si = \sum_{i=0}^{3}(4-i)\cdot X_i \qquad (2)$$

The mole fraction of different structural units (X_i) is related to pertinent peak areas [41], as expressed by the following Equation (3),

$$X_i = \theta_i \cdot A_i \qquad (3)$$

where θ_i and A_i represent the Raman scattering coefficient and peak area of the

structural unit, respectively. The values of θ_i (i=0, 1, 2 and 3) are equal to 1, 0.514, 0.242 and 0.09, respectively [41, 42].

Figure 5 (c) plots the variations of NBO/Si and mole ratios of Q^3 to Q^2 (X_3/X_2) with different Al_2O_3/SiO_2 mass ratios. It reveals that there has been a gradual decline in the estimated X_3/X_2 ratio, whereas the calculated NBO/Si demonstrates an upward trend, indicating the gross depolymerization of the flux network is enhanced by the increase of the Al_2O_3/SiO_2 mass ratio. It is worth noting that the enhancement of NBO/Si is less pronounced for fluxes with Al_2O_3/SiO_2 mass ratios higher than 0.9 (flux F4), which corresponds to the gentle trend of viscosity change.

3.4 MD simulation

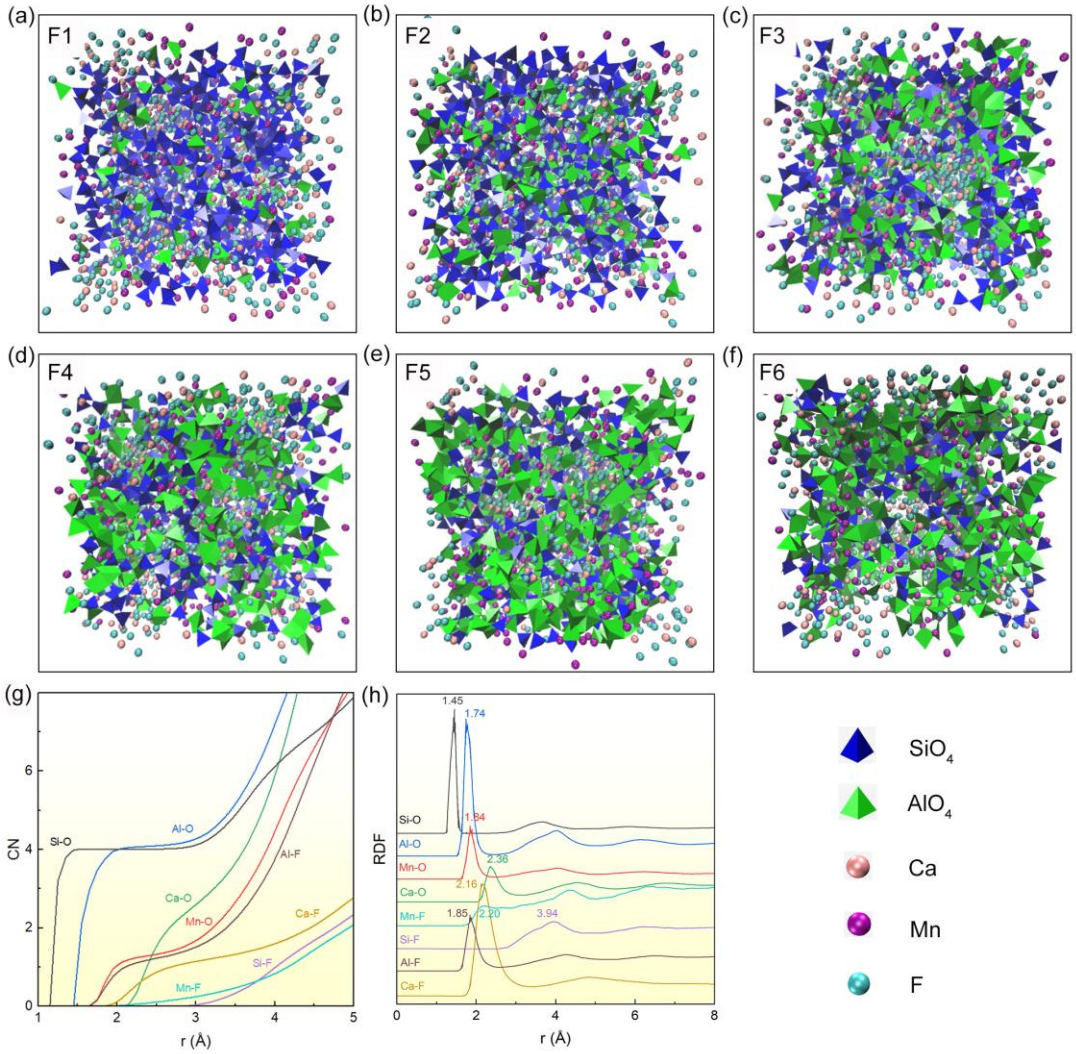

Figure 6 (a)-(f) Atomic configuration of different fluxes, (g) typical variations of coordination number (CN) for bonds between different atoms, and (h) typical variations of radial distribution function (RDF) for bonds between different atoms.

Figure 6 (a)-(f) illustrates the atomic configuration of fluxes with different Al_2O_3/SiO_2 mass ratios. It was evidently observed that the number of [SiO_4]-tetrahedral units decreases and that of [AlO_4]-tetrahedral units increases with increasing Al_2O_3/SiO_2 mass ratio. The molecular radial distribution function (RDF) and molecular

coordination number (CN) curves of each atom can be obtained statistically from the above MD simulations. Typical RDF and CN curves (F6) are shown in Figure 6(g) and 6(h). (The RDF and CN curves of other samples are shown in Supplemental Materials Figure S4.) As can be seen in Figure 6(g), CN_{Si-O} and CN_{Al-O} have a plateau at the ordinate value of 4, which indicates that the coordination numbers of Si-O and Al-O are both 4, suggesting the formation of $[SiO_4]$- and $[AlO_4]$-tetrahedral units, respectively [43]. The RDF curves shown in Figure 6(h) imply that Si-O and Al-O with adjacent sharp peaks can be substituted with each other to form aluminosilicate structures [24]. For F-related bonds, compared with Si-F and Mn-F in the CN curves, the platforms of Al-F and Ca-F are more obvious, indicating higher probability for the existence of Al-F and Ca-F in the network structure. In addition, Al-F and Ca-F structures with apparent peaks and Si-F and Mn-F structures without obvious peaks in the RDF curves suggest that F-related structures are mostly Al-F and Ca-F [7, 44].

Based on the above discussion, it can be inferred that Al^{3+} in the flux system does not exhibit amphoteric behavior, and the flux system gradually changes from a silicate structure to an aluminosilicate structure, which reduces the bond energy and lowers the viscosity. Furthermore, the absence of Si-F and the presence of Al-F demonstrate the transformation from the $Al\text{-}O^-$ structure to the Al-F structure, which further reduces the degree of polymerization of the flux system [45].

3.5 Viscosity and structure analysis from thermodynamic view

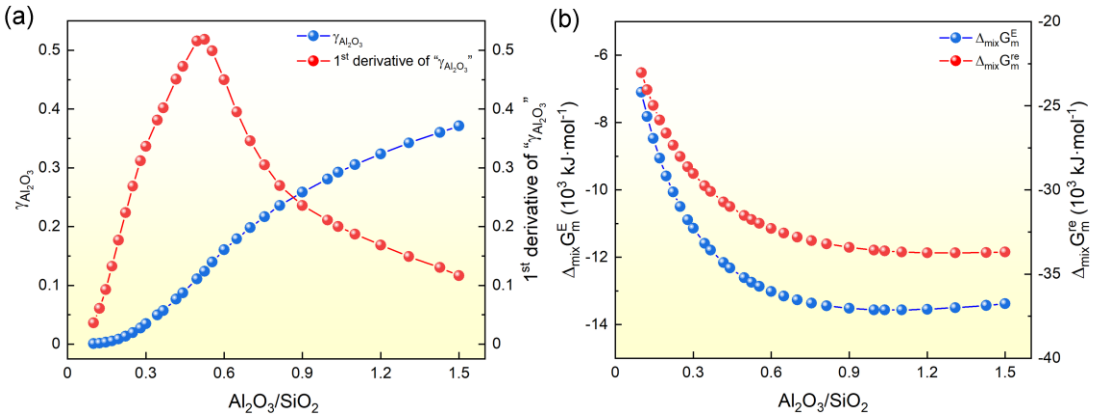

Figure 7 (a) Activity coefficient of Al_2O_3 in SiO_2-MnO-CaF_2-Al_2O_3 welding flux as a function of Al_2O_3/SiO_2 mass ratio at 1500 °C, and (b) change of molar excess Gibbs free energy and molar Gibbs free energy of real solution with the variation of Al_2O_3/SiO_2 mass ratio at 1500 °C.

Flux viscous behaviors and structural changes are essentially governed by thermodynamics [18]. Activity coefficient and molar excess Gibbs free energy ($\Delta_{mix}G_m^E$) can perform deviations from the ideal solution, and the molar Gibbs free energy of real solution ($\Delta_{mix}G_m^{re}$) can reflect the stability of the actural flux system [46, 47]. Activity values (a_i) of the fluxes were calculated by FactSage 8.1. Relevant thermodynamic parameters can be calculated from Equations (5)-(7):

$$\gamma_i = {}^{a_i}/_{x_i} \quad (5)$$

$$\Delta_{mix}G_m^E = RT\sum_{i=1}^{n} x_i \ln \gamma_i \quad (6)$$

$$\Delta_{mix}G_m^{re} = RT\sum_{i=1}^{n} x_i \ln a_i \quad (7)$$

where γ_i is the activity coefficient, x_i is the mole fraction, R is molar gas constant, and T is temperature in K.

303 Figure 7 (a) offers the variation of activity coefficient of Al_2O_3 and its first
304 derivative with increase of Al_2O_3/SiO_2 mass ratio at 1500 °C. It could be observed that
305 the activity coefficient of Al_2O_3 increases with increasing Al_2O_3/SiO_2 mass ratio and its
306 upward trajectory follows an approximately "S"-shaped curve. The first derivative of
307 the "S"-shaped curve reaches the inflection point with an approximate Al_2O_3/SiO_2 mass
308 ratio of 0.5, indicating a transformation from silicate-dominant structure to
309 aluminosilicate structure [48].

310 The activity coefficient of Al_2O_3 indicates the degree of deviation from the ideal
311 state, which, in turn, sketches the degree of confinement of the minor network former
312 Al_2O_3 by the major network former SiO_2 [18]. It can also be seen from Figure 7(a) that
313 the activity coefficient of Al_2O_3 increases with the decrease of SiO_2, indicating an
314 increasingly dominating role of Al_2O_3 in the flux structure. Thus, when the Al_2O_3/SiO_2
315 mass ratio is less than 0.5, Si-bearing banding vibration in $[SiO_4]$-structural units plays
316 a dominant role. While the Al_2O_3/SiO_2 mass ratio is greater than 0.5, the whole structure
317 undergoes depolymerization, generating more Si-O-Al bonds and $[AlO_4]$-tetrahedral
318 units. Considering that intermolecular forces can determine the overall strength of the
319 network structure, the weaker bond energy of Al-O, as compared with that of Si-O,
320 could further reduces the viscosity of the flux system [40].

321 Figure 7 (b) exhibits the variation of the molar Gibbs free energy of real mixing and
322 molar excess Gibbs free energy of the flux system at 1500 °C with incremental
323 Al_2O_3/SiO_2 mass ratio. It can be seen that molar excess Gibbs free energy and molar
324 Gibbs free energy of the real solution drop abruptly with the initial increase of

Al_2O_3/SiO_2 mass ratio, as caused by the breakage of the dominant Si-O bonds and the appearance of more Al^{3+} requiring charge compensation during this process. It indicates that a deviation from the ideal state reaches a maximum value as the Al_2O_3/SiO_2 mass ratio increases to 0.9, accompanied by the generation of a minimum value of molar excess Gibbs free energy. Thus, an apparently restrained downward trend of viscosity was observed with further increasing Al_2O_3/SiO_2 mass ratios from 0.9 to 1.5.

4 Conclusions

In this study, morphological changes of weld metals and slag shells treated by SiO_2-MnO-CaF_2-Al_2O_3 welding fluxes with varied Al_2O_3/SiO_2 mass ratios have been elucidated from viscosity and structure perspectives. The following conclusions could be obtained.

(1) Surface quality of the weld metal ameliorates and slag detachability improves as the Al_2O_3/SiO_2 mass ratio increases, which matches well with viscosity changing trajectory.

(2) The estimated Q^3/Q^2 (X_3/X_2) ratio reveals a gradual decline trend, whereas the calculated NBO/Si demonstrates an upward trend with the increase of Al_2O_3/SiO_2 mass ratio, indicating enhanced depolymerization of the flux network.

(3) Molecular dynamics simulation indicates fluxes transform from silicate structure to aluminosilicate structure. F prefers to link with Al and Ca to reduce the overall degree of polymerization.

(4) Thermodynamic analysis indicates that the formation of [AlO_4]-tetrahedral units

and Si-O-Al bonds leads to a minimum molar excess Gibbs free energy when the Al_2O_3/SiO_2 mass ratio is 0.9, and further increase of the Al_2O_3/SiO_2 mass ratio has little effect on viscosity.

Acknowledgments

The authors sincerely thank the National Natural Science Foundation of China (Grant Nos. U20A20277, 52104295, 52050410341, 52150610494), National Key Research and Development Program of China (Grant No. 2022YFE0123300), Young Elite Scientists Sponsorship Program by CAST (YESS) (Grant No. 2021-2023QNRC001) and Research Fund for Central Universities (Grant Nos. N2025025, N2125016).

Supporting information

Additional supporting information may be found online in the Supporting Information section at the end of the article.

CRediT authorship contribution statement

Zhanjun Wang: Data curation, Formal analysis, Methodology, Writing - review & editing; **Zuohong Li**: Data curation, Writing - original draft; **Ming Zhong**: Writing - review; **Zushu Li**: Writing - review; **Cong Wang**: Supervision, Resources, Writing - review & editing, Funding acquisition.

Declaration of Competing Interest

The authors declare that they have no known competing financial interests or personal relationships that could have appeared to influence the work reported in this paper.

References

[1] X. Yuan, M. Zhong, Y. Wu, C. Wang, Characterizing inclusions in the weld metal of EH36 shipbuilding steel processed by CaF_2-30 wt pct TiO_2 flux, Metall. Mater. Trans. B, 53 (2022) 656-661.

[2] Y. Wu, X. Yuan, I. Kaldre, M. Zhong, Z. Wang, C. Wang, TiO_2-assisted microstructural variations in the weld metal of EH36 shipbuilding steel subject to high heat input submerged arc welding, Metall. Mater. Trans. B, (2020) Accepted.

[3] J.Y. Park, S.J. Park, W.S. Chang, I. Sohn, Effect of FeO_t content and CaO/SiO_2 ratio on hydrogen dissolution in CaF_2–CaO–SiO_2-based welding fluxes, J. Am. Ceram. Soc., 95 (2012) 1756-1763.

[4] J.B. Kim, J.K. Choi, I.W. Han, I. Sohn, High-temperature wettability and structure of the TiO_2–MnO–SiO_2–Al_2O_3 welding flux system, J. Non-Cryst. Solids, 432 (2016) 218-226.

[5] C. Wang, J. Zhang, Fine-tuning weld metal compositions via flux optimization in submerged arc welding: an overview, Acta Metall Sin, 57 (2021) 1126-1140.

[6] X. Xie, M. Zhong, T. Zhao, C. Wang, Probing microstructural evolution in weld metals subjected to varied CaF_2–TiO_2 flux cored wires under high heat input electro-gas welding, J. Iron Steel Res. Int., (2022) https://doi.org/10.1007/s42243-42022-00814-42243.

[7] Z. Wang, Y. Liu, M. Zhong, Z. Li, C. Wang, Bubble evolution behaviors induced by CaO–Al_2O_3–SiO_2–CaF_2 fluxes subjected to high heat input submerged arc

welding, Metall. Mater. Trans. B, 53 (2022) 2763-2767.

[8] T. Coetsee, F. De Bruin, In situ modification of CaF_2-SiO_2-Al_2O_3-MgO flux applied in the aluminium-assisted transfer of titanium in the submerged arc welding of carbon steel: process mineralogy and thermochemical analysis, Minerals, 12 (2022) 604.

[9] P.F. Mendez, T.W. Eagar, Welding processes for aeronautics, Adv. Mater. Processes, 159 (2001) 39-43.

[10] J. Zhang, C. Wang, T. Coetsee, Thermodynamic evaluation of element transfer behaviors for fused CaO-SiO_2-MnO fluxes subjected to high heat input submerged arc welding, Metall. Mater. Trans. B, 52 (2021) 1937-1944.

[11] C.S. Chai, T.W. Eagar, Slag-metal equilibrium during submerged arc welding, Metall. Mater. Trans. B, 12 (1981) 539-547.

[12] J.B. Kim, I. Sohn, Influence of TiO_2/SiO_2 and MnO on the viscosity and structure in the TiO_2-MnO-SiO_2 welding flux system, J. Non-Cryst. Solids, 379 (2013) 235-243.

[13] J.B. Kim, I. Sohn, Effect of SiO_2/Al_2O_3 and TiO_2/SiO_2 ratios on the viscosity and structure of the TiO_2-MnO-SiO_2-Al_2O_3 welding flux system, ISIJ Int., 54 (2014) 2050-2058.

[14] Z. Wang, J. Zhang, M. Zhong, C. Wang, Insight into the viscosity–structure relationship of MnO-SiO_2-MgO-Al_2O_3 fused submerged arc welding flux, Metall. Mater. Trans. B, 53 (2022) 1364-1370.

[15] J.Y. Park, I. Sohn, The effects of CaF_2, basicity, and atmospheric conditions on the solubility of carbon and nitrogen in the CaO-SiO_2-Al_2O_3-based slag system, Metall. Mater. Trans. B, 44 (2013) 123-132.

[16] Z. Wang, X. Zheng, M. Zhong, Z. Li, C. Wang, Crystallization behavior of CaF_2-TiO_2 fluxes geared towards high heat input submerged arc welding, J. Non-Cryst. Solids, 591 (2022) 121716.

[17] X. Yuan, Y. Wu, M. Zhong, S. Basu, Z. Wang, C. Wang, Profiling inclusion characteristics in submerged arc welded metals of EH36 shipbuilding steel

treated by CaF_2-TiO_2 fluxes, Sci. Technol. Weld. Joi., 27 (2022) 683-690.

[18] Z. Chen, H. Wang, Y. Sun, L. Liu, X. Wang, Insight into the relationship between viscosity and structure of CaO-SiO_2-MgO-Al_2O_3 molten slags, Metall. Mater. Trans. B, 50 (2019) 2930-2941.

[19] H. Tian, Z. Wang, T. Zhao, C. Wang, A Raman and multinuclear ^{29}Si, ^{27}Al, and ^{19}F NMR study on the structural roles of CaF_2 in SiO_2–CaO–Al_2O_3-based welding fluxes, Metall. Mater. Trans. B, 53 (2022) 232-241.

[20] Z. Wang, I. Sohn, Effect of substituting CaO with BaO on the viscosity and structure of CaO-BaO-SiO_2-MgO-Al_2O_3 slags, J. Am. Ceram. Soc., 101 (2018) 4285-4296.

[21] T.S. Kim, J.H. Park, Viscosity-structure relationship of alkaline earth silicate melts containing manganese oxide and calcium fluoride, J. Am. Ceram. Soc., 102 (2019) 4943-4955.

[22] J. Yang, Z. Wang, I. Sohn, Topological understanding of thermal conductivity in synthetic slag melts for energy recovery: An experimental and molecular dynamic simulation study, Acta Mater., 234 (2022) 118014.

[23] C. Jiang, K. Li, J. Zhang, Q. Qin, Z. Liu, W. Liang, M. Sun, Z. Wang, The effect of CaO (MgO) on the structure and properties of aluminosilicate system by molecular dynamics simulation, J. Mol. Liq., 268 (2018) 762-769.

[24] Z. Wang, S. Cai, M. Zhang, M. Guo, Z. Zhang, Structural investigation of phosphorus in CaO-SiO_2-P_2O_5 ternary glass, Metal. Metar. Trans. B, 48 (2017) 1139-1148.

[25] H. Wang, R. Qin, G. He, SiO_2 and CaF_2 behavior during shielded metal arc welding and their effect on slag detachability of the CaO-CaF_2-SiO_2 type ENiCrFe-7-covered electrode, Metall. Mater. Trans. A, 47 (2016) 4530-4542.

[26] J. Kim, T. Lee, I. Sohn, Effect of compositional variation in TiO_2-based flux-cored arc welding fluxes on the thermo-physical properties and mechanical behavior of a weld zone, Metall. Mater. Trans. A, 49 (2018) 2705-2720.

[27] J. Liao, Y. Zhang, S. Sridhar, X. Wang, Z. Zhang, Effect of Al_2O_3/SiO_2 ratio on

448 the viscosity and structure of slags, ISIJ Int., 52 (2012) 753-758.
449 [28] C. Jackson, The science of arc welding, Weld. J., 2 (1960) 129-140.
450 [29] B. Singh, Z.A. Khan, A.N. Siddiquee, Review on effect of flux composition on
451 its behavior and bead geometry in submerged arc welding (SAW), Am. J. Mech.
452 Eng., 5 (2013) 123-127.
453 [30] C.B. Dallam, S. Liu, D.L. Olson, Flux composition dependence of
454 microstructure and toughness of submerged arc hsla weldments, Weld. J., 64
455 (1985) 140-151.
456 [31] B. Chai, T.W. Eacar, Slag metal reactions in binary CaF_2-metal oxide welding
457 fluxes, Weld. J., 61 (1982) 229-232.
458 [32] J.H. Park, D.J. Min, H.S. Song, FT-IR spectroscopic study on structure of CaO-
459 SiO_2 and CaO-SiO_2-CaF_2 slags, ISIJ Int., 42 (2002) 344-351.
460 [33] J.B. Kim, I. Sohn, Effect of SiO_2/Al_2O_3 and TiO_2/SiO_2 ratios on the viscosity and
461 structure of the TiO_2–MnO–SiO_2–Al_2O_3 welding flux system, ISIJ Int., 54 (2014)
462 2050-2058.
463 [34] H. Shao, E. Gao, W. Wang, L. Zhang, Effect of fluorine and CaO/Al_2O_3 mass
464 ratio on the viscosity and structure of CaO-Al_2O_3-based mold fluxes, J. Am.
465 Ceram. Soc., 102 (2019) 4440-4449.
466 [35] C. Huang, E.C. Behrman, Structure and properties of calcium aluminosilicate
467 glasses, J. Non-Cryst. Solids, 128 (1991) 310-321.
468 [36] W. Liu, Y. Chen, J. Chen, J. Wang, H. Zuo, Viscosity and structure evolution of
469 bearing-BaO slag melt with the low CaO/SiO_2 mass ratio of 0.7, J. Am. Ceram.
470 Soc., 105 (2022) 842-852.
471 [37] M. Paul, Structural studies of silicate glasses and melts—applications and
472 limitations of Raman spectroscopy, Am. Mineral., 69 (1984) 622-644.
473 [38] B.O. Mysen, D. Virgo, C.M. Scarfe, Relations between the anionic structure and
474 viscosity of silicate melts-a Raman spectroscopic study, Am. Mineral., 65 (1980)
475 690-710.
476 [39] M. Paul, P. Bernard, Raman spectroscopy of calcium aluminate glasses and

crystals, J. Non-Cryst. Solids, 55 (1983) 221-242.

[40] Z. Wang, I. Sohn, Effect of substituting CaO with BaO on the viscosity and structure of CaO-BaO-SiO_2-MgO-Al_2O_3 slags, J. Am. Ceram. Soc., 101 (2018) 4285-4296.

[41] K. Zheng, J. Liao, X. Wang, Z. Zhang, Raman spectroscopic study of the structural properties of CaO-MgO-SiO_2-TiO_2 slags, J. Non-Cryst. Solids, 376 (2013) 209-215.

[42] W. Wang, S. Dai, L. Zhou, J. Zhang, W. Tian, J. Xu, Viscosity and structure of MgO–SiO_2-based slag melt with varying B_2O_3 content, Ceram. Int., 46 (2020) 3631-3636.

[43] X. He, S. Ma, L. Wang, H. Dong, K. Chou, Comparison of desulfurization mechanism in liquid CaO-SiO_2 and MnO-SiO_2: An ab initio molecular dynamics simulation, J. Alloy Compd., 896 (2022) 163008.

[44] Z. Wang, Y. Sun, S. Seetharaman, M. Zhang, M. Guo, Z. Guo, Z. Zhang, Viscous flow and crystallization behaviors of P-bearing steelmaking slags with varying fluorine content, ISIJ Int., 56 (2016) 546-553.

[45] J. Gao, G. Wen, T. Huang, B. Bai, P. Tang, Q. Liu, Effect of Al speciation on the structure of high-Al steels mold fluxes containing fluoride, J. Am. Ceram. Soc., 99 (2016) 3941-3947.

[46] V.L. Stolyarova, Thermodynamic properties and structure of ternary silicate glass-forming melts: Experimental studies and modeling, J. Non-Cryst. Solids, 354 (2008) 1373-1377.

[47] A. Shankar, M. Gornerup, A.K. Lahiri, S. Seetharaman, Experimental investigation of the viscosities in CaO-SiO_2-MgO-Al_2O_3 and CaO-SiO_2-MgO-Al_2O_3-TiO_2 slags, Metall. Mater. Trans. B, 38 (2007) 911-915.

[48] W. Zhang, F. He, Y. Xiao, M. Xie, F. Li, J. Xie, H. Yang, Z. Li, Structure, viscosity, and crystallization of glass melt from molten blast furnace slag, Int. J. Appl. Glass Sci., 11 (2020) 676-684.

Figure and Table captions:

Table 1 Chemical compositions (wt.%) of the designed fluxes.

Figure 1 Macrographs of WMs and corresponding separated slag shells treated by different fluxes.

Figure 2 Viscosity of SiO_2-MnO-CaF_2-Al_2O_3 fluxes as a function of Al_2O_3/SiO_2 mass ratio obtained at various temperatures.

Figure 3 (a) FTIR absorption spectra of all SiO_2-MnO-CaF_2-Al_2O_3 fluxes with various Al_2O_3/SiO_2 mass ratios, and (b) FTIR intensity contour map of SiO_2-MnO-CaF_2-Al_2O_3 fluxes.

Figure 4 (a) Raman spectra of the fluxes with various Al_2O_3/SiO_2 mass ratios, and (b) Raman intensity contour map of SiO_2-MnO-CaF_2-Al_2O_3 fluxes.

Figure 5 (a) Typical deconvolution result of Raman spectra, (b) area fraction of the characteristic [SiO_4]-tetrahedral units, and (c) variation of NBO/Si and Q^3/Q^2 mole ratios in SiO_2-MnO-CaF_2-Al_2O_3 fluxes.

Figure 6 (a)-(f) Atomic configuration of different fluxes, (g) typical variations of coordination number (CN) for bonds between different atoms, and (h) typical variations of radial distribution function (RDF) for bonds between different atoms.

Figure 7 (a) Activity coefficient of Al_2O_3 in SiO_2-MnO-CaF_2-Al_2O_3 welding flux as a

function of Al_2O_3/SiO_2 mass ratio at 1500 °C, and (b) change of molar excess Gibbs free energy and molar Gibbs free energy of real solution with the variation of Al_2O_3/SiO_2 mass ratio at 1500 °C.